

## 4 THE IMPACT OF GRAIN SIZE

### ACTIVATION ENERGY AND MIGRATION PATHWAYS IN MAPbBr<sub>3</sub> SOLAR CELLS

Ion migration in perovskite layers can significantly reduce the long-term stability of the devices. While perovskite composition engineering has proven an interesting tool to mitigate ion migration, many optoelectronic devices require a specific bandgap and thus require a specific perovskite composition. Here, we look at the effect of grain size to mitigate ion migration. We find that in MAPbBr<sub>3</sub> solar cells prepared with grain sizes varying from 2 to 11  $\mu\text{m}$ , the activation energy for bromide ion migration increases from 0.17 to 0.28 eV. Moreover, we observe the appearance of a second bromide ion migration pathway for the devices with largest grain size, which we attribute to ion migration mediated by the bulk of the perovskite, as opposed to ion migration mediated by the grain boundaries. Together, these results suggest the beneficial nature of grain engineering for reduction of ion migration in perovskite solar cells.

This chapter is based on the following publication<sup>124</sup>:  
Lucie McGovern, Isabel Koschany, Gianluca Grimaldi, Loreta A. Muscarella and Bruno Ehrler, "Grain Size Influences Activation Energy and Migration Pathways in MAPbBr<sub>3</sub> Perovskite Solar Cells", *Journal of Physical Chemistry Letters*, vol. 12, pp. 2423–2428, 2021.

## 4.1 INTRODUCTION

Over the recent decade, the advancement of metal halide perovskite solar cells has shown remarkable results, with power conversion efficiencies (PCEs) reaching as high as 25.5 % for single junctions and 29.2 % for perovskite/silicon tandems<sup>10</sup>. In terms of efficiency, this class of material has thus proven effective in solar cell devices. This high performance is, however, somewhat mitigated by the stability issue this technology currently exhibits, where a decrease of the PCE of devices over time is commonly observed. This stability loss can be linked to two types of degradation processes, caused by either intrinsic factors or extrinsic factors. Extrinsic factors include moisture, oxygen exposure, and heat, which can all rapidly degrade the PCE of devices. Though very detrimental to cell performance, these degradation-inducing factors can mostly be prevented, noticeably through passivation or encapsulation schemes of the perovskite layer<sup>140–143</sup>. Of more problematic nature are the intrinsic factors of degradation. Indeed, contrary to most solar cell technologies, perovskite crystals are not formed by covalent bonds only, but instead exhibit dual covalent and ionic nature<sup>12,144</sup>, bearing in mind that ionic bonds are weaker. A number of defects can thus readily occur in the perovskite lattice, including ion vacancies and ion interstitials<sup>33</sup>. Within the solar cell stack, these charged ions can drift toward the electrode of reverse polarity, in a process called ion migration. Under operation, this migration can further change the charge and elemental distribution throughout the perovskite layer and is known to affect the long-term stability of devices<sup>108,145,146</sup>.

To achieve long-term stability in metal halide perovskite solar cells, it is thus necessary to understand the intrinsic degradation process that is ion migration, to find suitable ways of mitigating and eventually suppressing this feature altogether.

In devices, the ions migrate from their initial defect position in the lattice toward the perovskite interface with the transport layer and accumulate at that interface<sup>89</sup>. However, there is still ongoing debate on how this migration proceeds in the film, namely, whether the process is mediated by the grain boundaries or rather by the bulk of the polycrystalline perovskite films. Some studies report an increased ion migration at grain boundaries, while others report the opposite effect: Studies reporting an enhancement of ion migration at grain boundaries include a range of atomic force microscopy techniques (c-AFM, KPFM, and BE-KPFM) showing the contact potential difference or the hysteresis per-

centage mapped locally<sup>48,147,148</sup>; imaging techniques (SEM) visualizing the deterioration of the grain boundaries<sup>148</sup>; elemental techniques (EDX) measuring the dynamic of the lead-to-halide ratio<sup>148</sup>; and conductivity measurements comparing films of various grain size to extract an activation energy for the migration process<sup>49</sup>. Studies reporting a reduction of ion migration at grain boundaries include PL techniques (PL microscopy and PLQY) tracking the ionic defect distribution rate<sup>149</sup> and intensity-modulated photocurrent spectroscopy measurements (IMPS) comparing the ionic current responses in thin and thick cells<sup>150</sup>.

With this study, we thus aim to answer the following question: is increasing the grain size an effective way to mitigate ion migration? We choose MAPbBr<sub>3</sub>, a well-characterized perovskite in terms of ion migration<sup>56,77,151</sup>. The major advantage of using this perovskite material is the possibility to synthesize films of varying grain size, without altering key physical or chemical properties of the film. To characterize and quantify ion migration, we use transient ion drift (TID), a capacitance-based technique which allows for determination of the nature of the mobile ions and quantification of their migration activation energy, diffusion coefficient, and number density<sup>51,56,76</sup>. The combination of this measurement technique together with a perovskite recipe that allows for grain size variation without any modification of the perovskite composition allows us to determine the influence of grain boundaries on ion migration in perovskite solar cells.

## 4.2 RESULTS AND DISCUSSION

### 4.2.1 VARYING THE GRAIN SIZE IN MAPbBr<sub>3</sub> SOLAR CELL DEVICES

To measure the influence of grain size on ion migration, we prepare solar cell devices with an active layer of polycrystalline MAPbBr<sub>3</sub> perovskite, of which we modulate the grain size. The recipe for MAPbBr<sub>3</sub> perovskite is adapted from reference [152]. Its advantage is the possibility of varying the perovskite grain size without modifying any key chemical parameters: only the spin-coating time is varied, while all other parameters, including precursor content, solvent, antisolvent, and annealing conditions, remain unchanged. Optical microscopy (OM) images of the films are shown in Figure 4.1a,b, where we observe that the grain size is correlated to the spinning time of the solution, with short spinning times leading to larger grains. After a spinning duration of 5 s, the grains in the final film

measure an average size of  $(11.3 \pm 1.7) \mu\text{m}$  (Figure 4.1a), while 60 s of spinning leads to an average size of  $(1.7 \pm 0.2) \mu\text{m}$  (Figure 4.1b). Grain size attribution by microscopy techniques such as OM and SEM might be misleading<sup>152,153</sup>; we thus confirm our initial OM characterization with electron backscatter diffraction (EBSD). The EBSD images show an overlay of the image quality (brightness, IQ) with the inverse pole figure (color, IPF) along the  $z$ -axis (normal to the substrate, Figure 4.1c,d) and  $x$ -axis (parallel to the substrate, Figure 4.1e,f). The IPF relative to the  $x$ -axis shows a distribution of orientations along the  $[101]$  and the  $[111]$  directions, indicative of polycrystallinity. The grains and grain boundaries detected by EBSD correspond to those observed by OM, thereby confirming the grain size characterization by OM. We conclude that this recipe, when used at spinning times between 5 and 60 s, allows for about 1 order of magnitude in grain size variation.

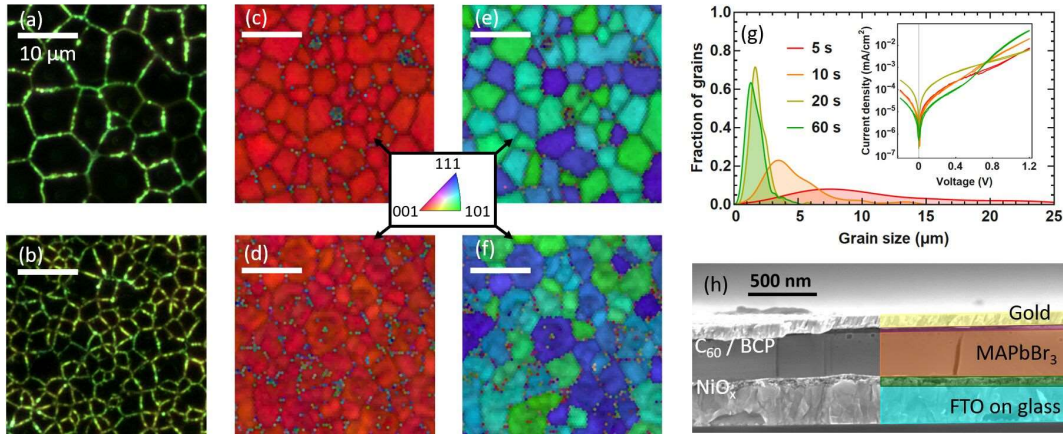


FIGURE 4.1. Top-view OM image of a  $\text{MAPbBr}_3$  perovskite film spin coated for (a) 5 s and (b) 60 s. The  $z$  orthogonal-direction top-view EBSD of the  $\text{MAPbBr}_3$  films spin coated for (c) 5 s and (d) 60 s. The  $x$  in-plane-direction top-view EBSD of the  $\text{MAPbBr}_3$  films spin coated for (e) 5 s and (f) 60 s. The inverse pole figure legend in the EBSD images shows the crystallization plane as a function of color. (g) Histogram of the average grain size as a function of spin coating time, with inset of the dark IV curves of the devices. (h) Cross-section SEM image showing the device layers: FTO,  $\text{NiO}_x$ ,  $\text{MAPbBr}_3$ ,  $\text{C}_{60}$ , BCP, and gold. The device has a planar p-i-n architecture. The white scale bars presented from (a) to (f) all represent a  $10 \mu\text{m}$  length.

The polydispersity in grain size is presented in the histogram in Figure 4.1g. The small grain regime is characterized by relatively sharp peaks of standard deviation  $\sim 0.2 \mu\text{m}$ , whereas the size distribution is more pronounced in the big grain regime, with standard deviations of 0.6 and

1.7  $\mu\text{m}$  respectively for the 5 and 11  $\mu\text{m}$  samples.

Each of these active perovskite layers of  $\text{MAPbBr}_3$  is incorporated into a p-i-n solar cell architecture as shown in Figure 4.1h. Representative cross-section SEM pictures show uniform stacking of these successive layers. The thick perovskite film exhibits vertical grain boundaries—the same as those observed in top-view OM images. The bottom electrode is a FTO layer, covered by a hole transport layer of  $\text{NiO}_x$  on top of which the  $\text{MAPbBr}_3$  perovskite is spin coated, finally the electron transport layer consists of  $\text{C}_{60}$  and BCP, and a gold electrode on top completes the device. The extraction layers are chosen specifically because they exhibit no direct ion migration, even though they may reduce the overall PCE of the devices. Dark IV curves of the devices (see the inset of Figure 4.1g) confirm good diode characteristics, a prerequisite for the TID measurements to study ion migration.

The solar cell performance of the devices is shown in Figure 4.2a, where the IV characteristics from the best cells are presented. There, it is already apparent that the FF and  $J_{\text{SC}}$  are the values most affected by grain size. For a fairer comparison, the average values taken over multiple pixels from multiple devices are shown in Table I. There, we observe that the  $V_{\text{OC}}$  does not change as a function of grain size, which is an indication that the amount of non-radiative recombination is similar in all devices. The overall PCE of the devices is constant through the series of varying grain size films: from 1 % to 1.3 %. The devices show reasonable efficiency for the simplistic solar cell architecture considered here, and are in line with other works using similar HTL and ETL<sup>79</sup>. As mentioned in above, we choose the extraction layers  $\text{NiO}_x$ ,  $\text{C}_{60}$  and BCP mainly because they are not themselves affected by ion migration, contrary to other commonly used extraction layers such as Li-TFSI doped Spiro-O-MeTAD<sup>45,154</sup>. We note that the low efficiency does not affect the TID measurement as the devices are measured in the dark where the measurement mainly requires a low dark current to avoid electrical charge flowing through the device affecting the depletion layer width. All in all, two parameters are thus affected by grain size,  $J_{\text{SC}}$  and FF, in an opposing manner, where the increase of one is concomitant to the decrease of the other – thereby maintaining a constant PCE. The relatively low fill factor values are partly due to a low shunt resistance. As mentioned earlier, this can be modulated by further device engineering and is therefore not the focus of the present study. The EQE curves of the devices are shown in Figure 4.2b. These match well with the corresponding IV curves of Figure 4.2a, with slightly lower  $J_{\text{SC}}$  values. The highest EQE point

	5 s	10 s	20 s	60 s
$J_{SC}$ (mA/cm <sup>2</sup> )	$4.1 \pm 0.2$	$3.2 \pm 0.1$	$3.6 \pm 0.2$	$4.3 \pm 0.3$
$V_{OC}$ (V)	$0.88 \pm 0.03$	$0.84 \pm 0.02$	$0.87 \pm 0.02$	$0.82 \pm 0.02$
FF (%)	$27.4 \pm 2.7$	$47.0 \pm 1.5$	$39.2 \pm 1.7$	$36.0 \pm 2.2$
PCE (%)	$1.0 \pm 0.1$	$1.3 \pm 0.1$	$1.2 \pm 0.1$	$1.3 \pm 0.1$

TABLE I. Average IV solar cell characteristics of the devices made with a polycrystalline MAPbBr<sub>3</sub> film prepared with a spin coating process of 5, 10, 20 or 60 seconds.

reaches almost 60 %, for the sample spin coated for 60 seconds (i.e. with smallest grain size). The overall shape of the EQE feature follows that of typical MAPbBr<sub>3</sub> absorption, with the characteristic excitonic peak at 525 nm, and the bandgap at 540 nm, further confirming the successful preparation of MAPbBr<sub>3</sub> devices.

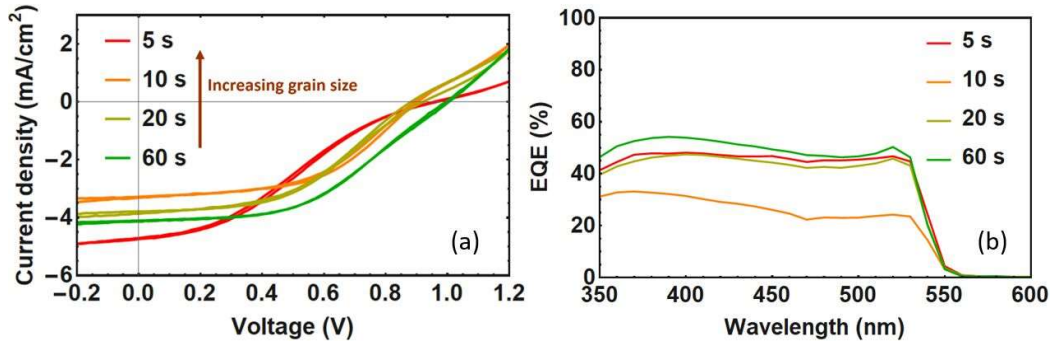


FIGURE 4.2. (a) Light IV curves of the best pixel for each of the solar cell device made with a photoactive layer of polycrystalline MAPbBr<sub>3</sub>, spin coated for 5, 10, 20 or 60 seconds. (b) EQE curves of the best pixels for each of these devices.

#### 4.2.2 TRANSIENT ION DRIFT CHARACTERISATION

TID is an electric spectroscopy technique for ion migration measurements used in perovskite solar cells<sup>56,76</sup>. The measurement is based on two steps: first, the application of a filling voltage which will redistribute the ions within a device and, second, the release of this voltage pulse, which will lead to the ions drifting back to their initial position. We record the capacitance signal during this second step by applying a small

alternating voltage  $V_{AC}$ , which thus provides a direct measurement of the ion migration process.

For TID characterization, the first step is the selection of a relevant frequency at which to apply the alternating voltage—for this purpose we measure the impedance spectra of all devices. The two extreme situations are presented in Figure 4.3, where the impedance spectra of the devices with smallest and largest grain size are shown respectively in panels a and b. Both impedance spectra look very much alike and resemble earlier measurements of  $\text{MAPbBr}_3$ <sup>56</sup>. They can be decomposed into a low-frequency regime which is temperature-dependent and dominated by ion accumulation<sup>155</sup> and a high-frequency regime which is characterized by a decrease of the capacitance signal due to the series resistance. In between these two regimes lies an intermediate plateau regime, where the capacitance is determined by the depletion capacitance - this is suitable for TID measurements. We thus select the frequency of  $10^4$  Hz for the small alternating voltage  $V_{AC}$  in the intermediate impedance regime.

Figures 4.3c and 4.3d show the TID capacitance traces after applying a filling voltage of 1 V for 2 s to the devices with smallest and largest grain size, respectively. Interestingly, both TID traces show a negative slope in the whole temperature range considered, independent of the grain size. This is further confirmed in the TID traces taken after applying filling voltages of 0.75 or 1.1 V (see Section 4.4.2). In TID of p-type semiconductors, a negative transient is attributed to anion migration. In the  $\text{MAPbBr}_3$  crystal structure, the only anion species is the bromide ion. The main ion migration process at play in the whole device range is thus bromide migration. This was previously observed for  $\text{MAPbBr}_3$  in our work comparing  $\text{MAPbI}_3$  and  $\text{MAPbBr}_3$ <sup>56</sup> and is further confirmed here.

#### 4.2.3 ACTIVATION ENERGY INCREASE, CONSTANT MOBILE ION DENSITY AND DIFFUSION COEFFICIENTS

In this study, we use TID to quantify the ion migration activation energy  $E_a$ , the density of mobile ions  $N_{ion}$ , and the diffusion coefficient  $D$  for each grain size. The fitting procedure is described in the Supporting Information, in Section 4.4.2, where the insets in Figure 4.3c,d show the good correspondence of the fits with the data.

In the small grain regime (1-3  $\mu\text{m}$ ), the data can be accurately fitted with one exponential contribution, suggesting a single ion migration process. As the average grain size grows ( $> 5 \mu\text{m}$ ), the fit needs an ad-



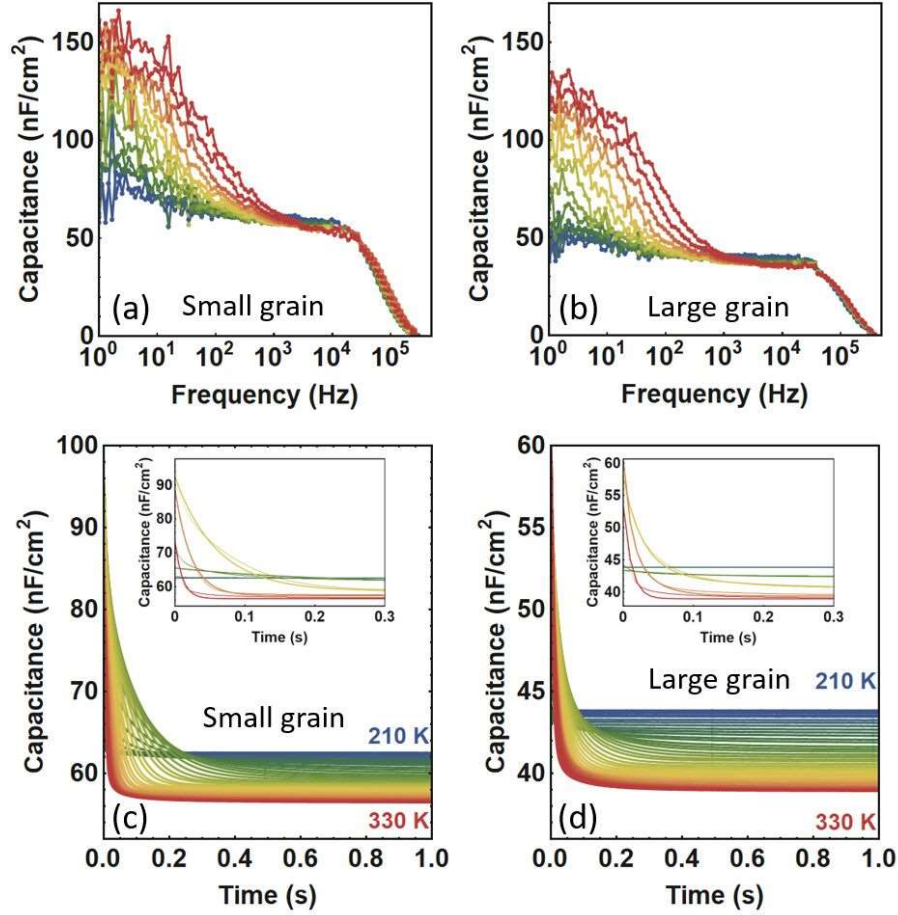


FIGURE 4.3. Impedance spectra of the devices with (a) 1.7  $\mu\text{m}$  and (b) 11.3  $\mu\text{m}$  grain size MAPbBr<sub>3</sub> perovskite films, measured by using an AC voltage of 10 mV. TID traces after applying a voltage pulse of 1 V for 2 s to the devices with (c) 1.7  $\mu\text{m}$  and (d) 11.3  $\mu\text{m}$  grain size perovskite films, between 210 and 330 K in steps of 3 K. The insets in (c) and (d) show the fit to the data for five intermediate temperatures: 210, 240, 270, 300, and 330 K.

ditional exponential contribution to accurately represent the data (see Figure 4.4a). TID cannot directly point to the microscopic migration pathway; however, the presence of two separate peaks (with distinct  $E_a$ ,  $N_{ion}$ , and  $D$ ) is a strong indication for the combination of two bromide migration processes in the perovskite film, where, for example, in addition to the grain boundary mediated pathway most often described, a bulk pathway would appear for films with larger grains. We expand on this idea below and for now refer to these migration pathways as peak A and peak B (respectively in purple and in orange in Figure 4.4).

The density of mobile ions is on the order of  $5 \times 10^{15} \text{ cm}^{-3}$  to



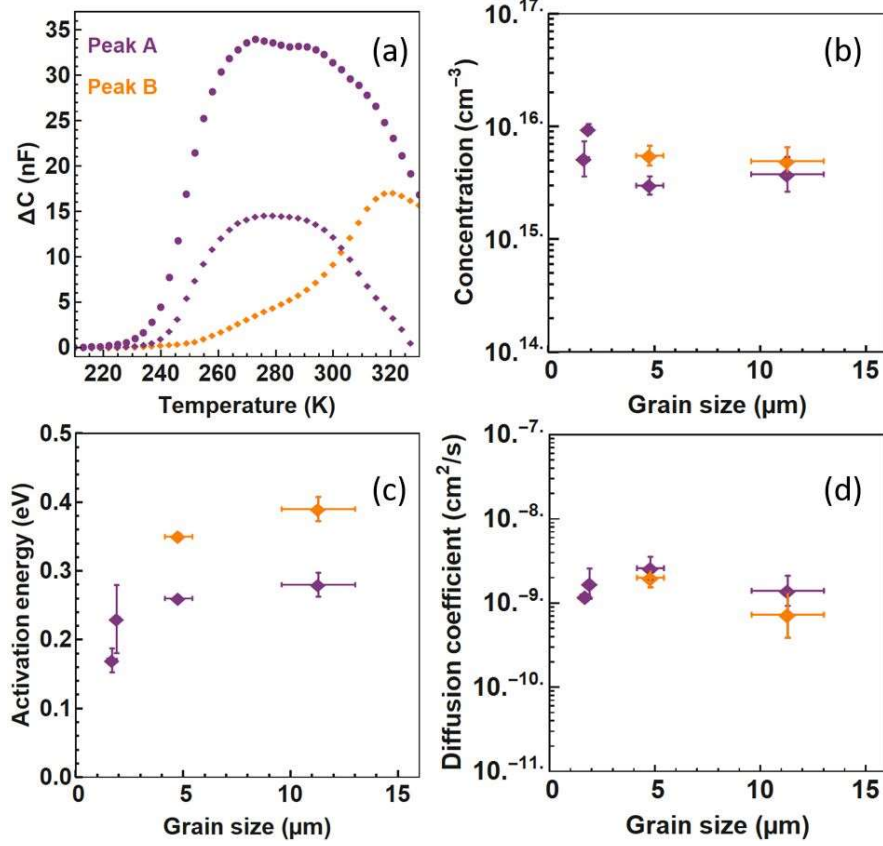


FIGURE 4.4. Effect of grain size on ion migration parameters: (a) Typical  $\Delta C$  peak(s) found after fitting the TID traces for samples with 1.7  $\mu\text{m}$  grain size (circle) and with 11  $\mu\text{m}$  grain size (diamond). Peaks A and B are shown in purple and orange, respectively. (b) Concentration of mobile ions, (c) activation energy, and (d) diffusion coefficient, extracted by using Equations in Section 4.4.2.

$1 \times 10^{16} \text{ cm}^{-3}$ , as shown in Figure 4.4b. We note that this low density of mobile ions is in agreement with the assumption of ions incompletely screening the built-in voltage in perovskites<sup>88</sup>. The total density of mobile species from peaks A and B is rather constant with grain size:  $5.2 \times 10^{15}$ ,  $9.5 \times 10^{15}$ ,  $8.5 \times 10^{15}$ , and  $8.7 \times 10^{15} \text{ cm}^{-3}$  for the samples with 1.7, 1.9, 4.8, and 11.3  $\mu\text{m}$  grain size, respectively. This is consistent with a model where the ion defect formation energy is independent of the grain size. This trend suggests that ion vacancies form in the bulk of the perovskite or at the interface with the transport layers.

We now look at the evolution of  $E_a$  as a function of grain size, as shown in Figure 4.4c. The activation energy describes the energy it

takes for an ion to move to the neighboring unit cell.  $E_a$  of peak A first strongly increases with grain size, before reaching a saturation regime for grains larger than 5  $\mu\text{m}$ . For peak B, which is only present for the larger grains, we notice a higher activation energy than peak A and a slight increase with grain size from  $(0.35 \pm 0.01)$  to  $(0.39 \pm 0.02)$  eV for films of average grain size 4.8 to 11.3  $\mu\text{m}$ . The general trend is thus an increase in the activation energy with grain size, indicative of a stronger barrier to the migration process for larger grains. This increase is first rapid and then reaches a saturation regime for grains between 5 and 11  $\mu\text{m}$ . We note that the defect formation energy (DFE) model developed by Meggiolaro *et al.*<sup>36</sup> shows a similar evolution of the activation energy with grain size but that a difference of DFE would lead to a change in the density of mobile ions in grain interiors compared to grain boundaries, an explanation which is in contradiction with our observation.

The diffusion coefficient as a function of grain size is presented in Figure 4.4d. The values are on the order of  $10^{-9} \text{ cm}^2 \text{ s}^{-1}$ , similar to previous observations for halide migration<sup>56</sup>. These remain relatively constant with grain size, the lowest value being observed for peak B of the sample with largest grains, with  $(7.3 \pm 4.6) \times 10^{-10} \text{ cm}^2 \text{ S}^{-1}$  and the highest value being observed for peak A of the sample with 4.8  $\mu\text{m}$  grains, with  $(2.6 \pm 0.8) \times 10^{-10} \text{ cm}^2 \text{ S}^{-1}$ . Within the error this shows a relatively constant diffusion coefficient as compared to the clear increase in activation energy with grain size. Additional considerations regarding the diffusion coefficient and activation energy trends are added in Section 4.4.2.

#### 4.2.4 GEOMETRICAL MODELLING

We now combine all the previous observations into a possible model. We find the same total number of mobile ions (from peaks A and B combined) independent of the grain size, which means that these mobile ions do not arise from the grain boundary. On top of that the activation energy of peak A increases with grain size. Here it cannot be explained by a reduced number of mobile ions in grain interiors compared to grain boundaries: this observation instead suggests that the mobile bromide ions experience a migration pathway with higher activation energy in the bulk of the grain relative to grain boundaries. We speculate that ions migrate first from their original location in the grain interior to the grain boundary and then through a grain boundary channel toward the interface. The larger the grain size, the fewer grain boundaries are present,

and the further away from a grain boundary an average ion will be positioned. The increase in activation energy of peak A with grain size is thus a representation of the longer average traveling distance to the grain boundary. The migration through the grain boundary channel is thus faster than the migration within the grain, in agreement with various experimental studies showing faster ion migration at the grain boundaries<sup>48,49,147,148</sup>. For larger grains we find a new ion migration pathway labeled peak B. With larger grains, it is possible that some of the ions migrating within the grain become so far away from any grain boundary that an additional migration pattern arises, where the ions migrate directly from the grain interior to the interface. The implication there is that the migration from grain interior to interface is slower than the migration from grain interior to grain boundary but still takes place when the interface becomes closer than a grain boundary region. This model is also consistent with a relatively constant activation energy and diffusion coefficient for peak B. The illustrative scheme of this model is presented in Figure 4.5a,b. We thus assign peak A as grain-boundary-mediated bromide migration and peak B as grain-interior-mediated bromide migration.

The observed trend can be approximately captured by a geometrical model for the motion of ions, in which, for simplicity, we consider the motion of ions along the fastest path to the electrode (see Section 4.4.3). Figure 4.5c shows the effective activation energy as a function of grain size, obtained by computing the fraction of the path occurring inside the grain and optimizing the value of the activation energies for bulk and grain boundaries diffusion. We obtain activation energies of 0.18 and 0.50 eV for ion diffusion along the grain boundaries and in the bulk. Despite the approximate nature of the model, leading to a large shift in the onset of the activation energy change as a function of grain size, it captures the experimentally observed increase in activation energy for larger grains.

We note that PL microscopy, PLQY, and IMPS studies<sup>149,150</sup> suggest that ions migrate from the inside of a grain to a grain boundary and then become trapped at the grain boundary. These works all have in common that they study ion migration along the in-plane direction by diffusion. Here, the ions may be initially trapped at the grain boundary, but they are then allowed to drift through the grain boundary channel in the normal direction, leading them to the interface of reverse polarity.

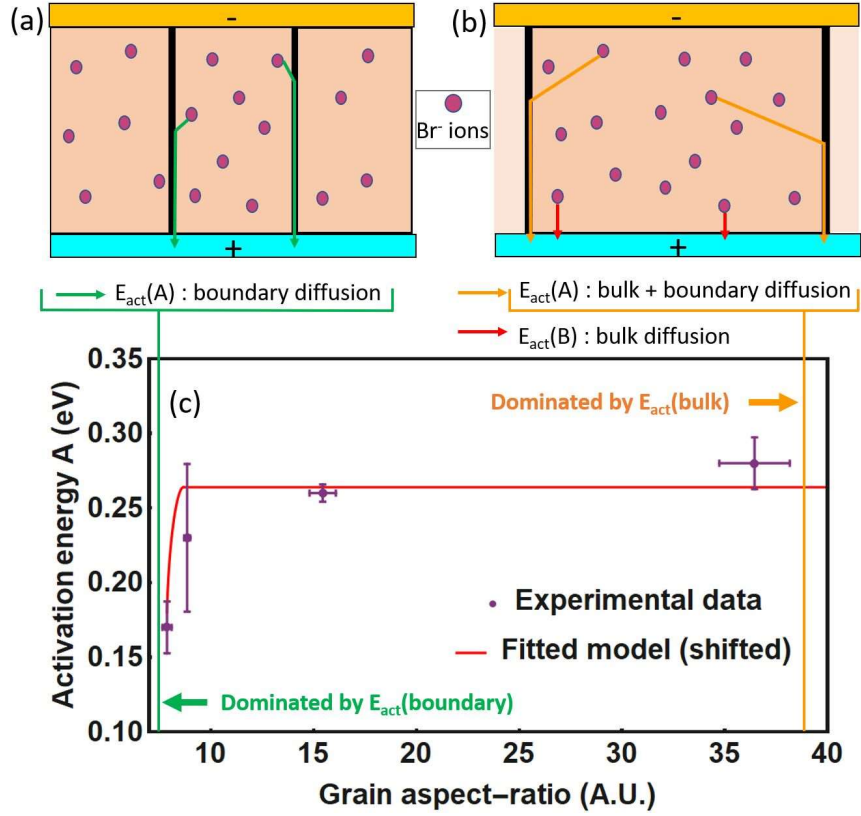


FIGURE 4.5. Model of ion migration in grains with different lateral size. Schematic of the proposed ion migration, where (a) in small grain sizes most ions first migrate to the grain boundary before they migrate to the interface via the boundary and (b) for larger grain sizes a second pathway appears where the ions migrate to the interface directly. (c) Fit to the experimental data of a geometrical model for the activation energy of ion diffusion (Section 4.4.4).

#### 4.2.5 TRAP STATES

The grain size of a perovskite film can also affect the electronic trap states. By applying a short voltage pulse of 20 ms instead of 2 s to measure only the contribution of trap states to the capacitance signal, we see changes in the trap state population and energy. The resulting trap depths, trap densities and trap attempt-to-escape frequencies of the MAPbBr<sub>3</sub> cells with smallest and largest grain size are presented in Table II.

We find one dominant electronic trap, which is shallower for the largest grain size sample ( $E_T = 192$  meV) compared to the smallest grain size ( $E_T = 300$  meV). This on its own could suggest an increase in the recombination rate for cells with smallest grain size. The density of traps

	5 s (largest grains)	60 s (smallest grains)
$E_{\text{trap}}$ (eV)	$0.192 \pm 0.020$	$0.300 \pm 0.002$
$N_{\text{trap}}$ ( $\text{cm}^{-3}$ )	$(1.55 \pm 0.64) \times 10^{15}$	$(7.25 \pm 0.18) \times 10^{15}$
$A(300 \text{ K})$ ( $\text{s}^{-1}$ )	$(4.58 \pm 0.11) \times 10^5$	$(7.86 \pm 0.74) \times 10^5$

TABLE II. Average trap depth, density of traps and attempt frequency of the devices made with a polycrystalline MAPbBr<sub>3</sub> film prepared with a spin coating process of 5 or 60 seconds (respectively with largest and smallest grain size).

is also highest for the cells with smallest grains, i.e. the cells with most grain boundaries. The factor of increase is a little over 4, close to the 3.8 difference in density of grain boundaries when going from cells with 1.7  $\mu\text{m}$  grains to cells with 11.3  $\mu\text{m}$  grains - this strongly suggests that the traps are located at the grain boundaries of the perovskite film. We thus find that the density of trap states scales with the number of grain boundaries present, suggesting that the grain boundaries play a major role in trap state formation. This initial finding warrants further investigation.

### 4.3 CONCLUSION

We studied bromide ion migration in MAPbBr<sub>3</sub> perovskite solar cells where we find that the grain size mainly affects the activation energy, while the density of mobile ions and their diffusion coefficient remain relatively constant with grain size. This is a first indication that crystallinity is indeed an effective tool to mitigate ion migration. The quantification of the density of mobile ions and diffusion coefficient are further useful in understanding how the migration pathway is affected by grain size. Ion migration is reduced in cells with larger grains not due to a lower density of mobile ions, but rather due to a higher energy of the transition state for the hopping process in the grain interior compared to that transition state at the grain boundary. Together, our results suggest that for smaller grains there is only one migration process mediated by the grain boundaries and that for larger grains a process mediated by the grain bulk becomes significant. Crystallinity is thus an effective tool to reduce ion migration, proving itself as an interesting strategy for long-term stability of devices.

## 4.4 APPENDIX

### 4.4.1 DEVICE FABRICATION AND CHARACTERISATION

The solar cell fabrication closely follows the recipes established in reference [56], with the notable exception of the MAPbBr<sub>3</sub> perovskite layer preparation, which we detail below.

The precursor for the MAPbBr<sub>3</sub> layer is fabricated from two solutions dissolved together in dimethyl sulfoxide (DMSO). First, a solution of 5.5 M methylamine hydro bromide (MABr, TCI) is made by dissolving the powder in DMSO (Sigma-Aldrich). To ensure a complete dissolution, the precursor is stirred and heated on a hot plate to 50-60 °C. The second precursor is a 1.8 M lead(II) acetate trihydrate (PbOAc) solution (Sigma-Aldrich). To prepare this solution, the PbOAc powder is dissolved in DMSO and stirred and heated to 50-60 °C overnight. Both precursor solutions are stirred and heated up to 65 °C until a clear dense solution is formed. This final MAPbBr<sub>3</sub> precursor solution has a molarity of 3.05 M. For the spin coating step, 200  $\mu$ L are used per sample, with a spin coating speed of 7500 rpm. To vary the grain size in the perovskite film, we vary the spin coating times: 5 s, 10 s, 20 s and 60 s. The samples are annealed for 1 h on the hot plate at 70 °C. During this annealing step, the samples quickly show a yellow-orange color, characteristic for MAPbBr<sub>3</sub>. All of the above steps are carried inside a glovebox in a nitrogen atmosphere, with an O<sub>2</sub> level below 1 ppm. For proper investigation both of the perovskite layer and of the full device, cells are either prepared until the perovskite layer (optical microscopy and EBSD imaging) or as the whole device (all electrical measurements and SEM cross-section imaging).

Optical microscopy images are taken using an Imager.A2m Zeiss microscope with an AxioCam ICc 5 camera in the dark field mode, with magnification objectives of 20  $\times$ , 50  $\times$  or 100  $\times$ . Many images of the various samples are collected and the evaluation of each grain size is done through software evaluation using the program ImageJ. Specifically, to characterize the polydispersity in grain size, we take OM pictures at multiple spots and of multiple films spin coated for the same duration. For each of these images we measure the average grain size. Performed over multiple images, we obtain statistics on the grain size distribution for about 60 to 80 grains per spin coating condition. We note that the word “grain size” used in this chapter systematically refers to grain diameter.

The SEM images are taken with a FEI Verios 460 scanning electron microscope in the secondary electron mode. The sample is cleaved in the

center to obtain the cross-section image. The acceleration voltage used is 10 kV and the working distance is 4 mm. EBSD images of MAPbBr<sub>3</sub> on NiO<sub>x</sub> are collected by using a direct electron detector based on the Timepix sensor from Amsterdam Scientific Instruments (ASI). The best parameters for the scans are found to be 10 keV for the voltage, 100 pA for the current, 50 ms for the exposure time, and between 10 and 12 mm for the working distances. The step size is chosen depending on the cluster size shown by the specific sample. EBSD data are collected using EDAX OIM software, and a Python script is used for image processing. The resulting Kikuchi patterns are indexed as cubic symmetry, using 1-3° as the degree of tolerance. Characterizing the MAPbBr<sub>3</sub> layer of the different spinning durations, we notice, on top of the grain size evolution, an evolution in the thickness of the perovskite layer. Samples prepared after 5 or 10 seconds spinning duration have a thickness of  $(310 \pm 10)$  nm, while the samples prepared after 20 or 60 seconds spinning duration have a thickness of  $(215 \pm 10)$  nm. This thickness difference is incorporated into the different Equations presented in Section 4.4.2 below.

#### 4.4.2 CAPACITANCE MEASUREMENTS

**GENERAL CONSIDERATIONS** For TID measurements the sample is loaded into a Janis VPF-100 liquid nitrogen cryostat inside a nitrogen-filled glovebox. Impedance spectroscopy, capacitance-voltage, transient ion-drift and deep level transient spectroscopy measurements are performed at a pressure below  $2 \times 10^{-6}$  mbar, in the dark, using a commercially available DLTS system from Semetrol. To ensure thermal equilibrium, the temperature of the sample is held constant for at least 30 minutes before impedance spectroscopy and capacitance-voltage measurements. Capacitance transient measurements were performed from 210 K to 330 K in steps of 3 K with a temperature accuracy of 0.2 K. The sample is held at 330 K for 30 minutes before starting the transient ion-drift and deep level transient spectroscopy measurements.

**MOTT-SCHOTTKY ANALYSIS** TID is a technique which makes use of a voltage bias to redistribute ions within a device. The voltage applied should thus be close to the built-in voltage of the cell. We determine this value by Mott-Schottky analysis<sup>155</sup> as shown in Figure 4.6. We obtain values of 1.09 V, 0.98 V, 1.02 V and 1.24 V for typical devices with grain size 1.7  $\mu$ m, 1.9  $\mu$ m, 4.8  $\mu$ m and 11.3  $\mu$ m, respectively. In the subsequent TID measurements, we thus apply voltage biases of 1 V (see Figure 4.3) and 1.1 V (see Figure 4.7). We further measure the devices with a lower



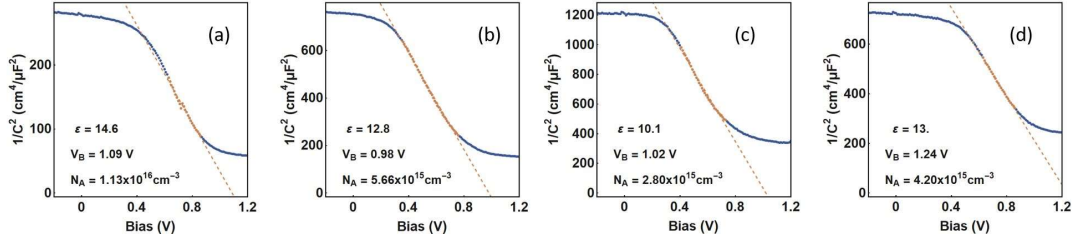


FIGURE 4.6. Mott-Schottky plots of the devices with MAPbBr<sub>3</sub> perovskite films of (a) 1.7  $\mu\text{m}$  grain size; (b) 1.9  $\mu\text{m}$  grain size; (c) 4.8  $\mu\text{m}$  grain size; (d) 11.3  $\mu\text{m}$  grain size.

applied voltage of 0.75 V in order to test the measurement response and to check if ion migration is already visible for smaller built-in fields. We note that our Mott-Schottky measurement is taken in reverse mode, and that the doping density values are found to be above the minimal threshold for correct Mott-Schottky evaluation<sup>98</sup>.

**STEADY-STATE CAPACITANCE** The steady-state capacitance (determined either by Thermal Admittance Spectroscopy (TAS) or by TID, taking the values at longer times) is found to be stable with temperature (see Figure 4.7 below). We attribute this effect to the choice of contact layers, NiO<sub>x</sub> and C<sub>60</sub>. Indeed, if we chose other contact layers, the geometric capacitance would become temperature dependent, presumably because of the formation of a dipole layer at that interface<sup>156</sup>.

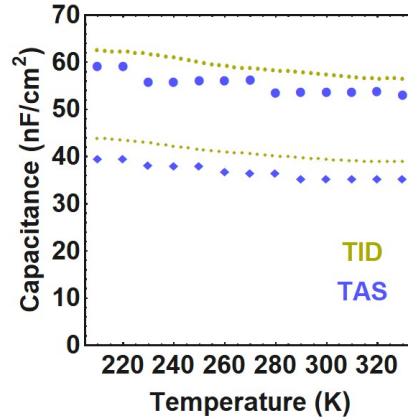


FIGURE 4.7. Steady-state capacitance values obtained by thermal admittance spectroscopy measurements at 10 kHz - in green - and from TID measurements, taking the capacitance value at longer times - in blue - for the cells with small and large grain size (represented by circle and diamond respectively).

**TID MEASUREMENTS WITH VARYING FILLING VOLTAGES** In Figure 4.8 a-h we show the TID traces taken at different filling voltages of 0.75 V and 1.1 V, for the samples from the smallest (Figure 4.7 a and e) to the largest grain size (Figure 4.7 d and h). The first observation is the presence of a similar trend in all cases, that is that the capacitance decreases with time. This pattern is conserved for the samples with small and large grain size, and for all filling voltages. The ion migration process at play must therefore remain bromide migration.

One parameter is, however, affected by the voltage pulse: the height of the transient, with higher voltages leading to a more pronounced transient. This indicates a difference in the density of mobile ions measured after applying the different filling voltages: more bromide mobile ions have been displaced when applying a voltage pulse of 1 V or 1.1 V, rather than a lower voltage pulse of 0.75 V. Some but not all of the mobile bromide ions in our devices have thus already been displaced by a voltage pulse of 0.75 V. This trend is consistent with a built-in voltage of about 1 V, meaning that the device is still partially depleted at 0.75 V.

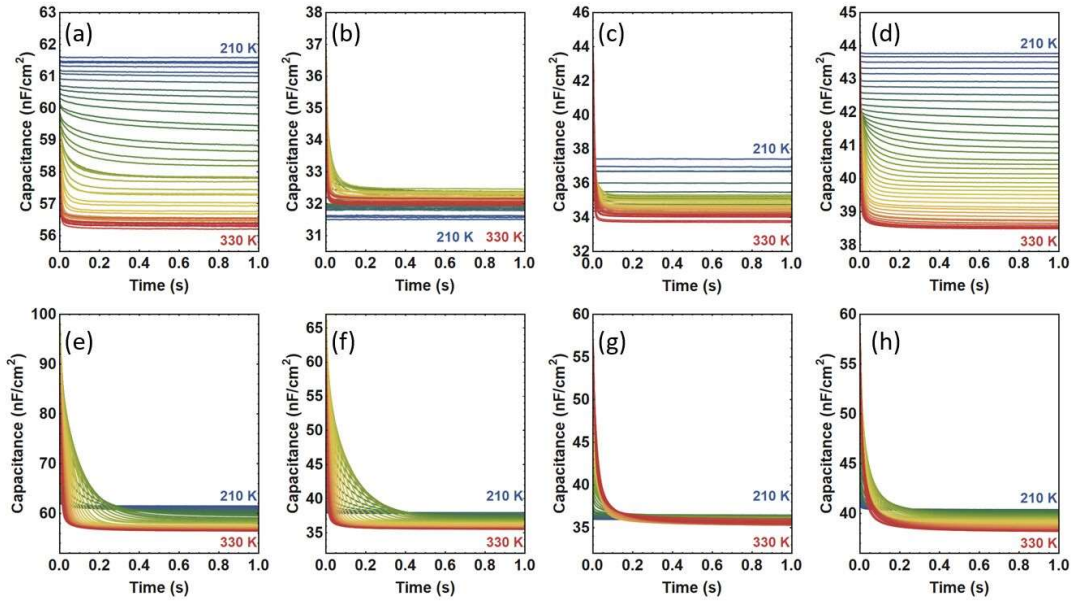


FIGURE 4.8. TID traces measured after applying filling voltage of 0.75 V for 2 seconds to the devices with MAPbBr<sub>3</sub> perovskite films of (a) 1.7  $\mu\text{m}$  grain size; (b) 1.9  $\mu\text{m}$  grain size; (c) 4.8  $\mu\text{m}$  grain size; (d) 11.3  $\mu\text{m}$  grain size; TID traces measured after applying a filling voltage of 1.1 V for 2 seconds to the devices with MAPbBr<sub>3</sub> perovskite films of (e) 1.7  $\mu\text{m}$  grain size; (f) 1.9  $\mu\text{m}$  grain size; (g) 4.8  $\mu\text{m}$  grain size; (h) 11.3  $\mu\text{m}$  grain size.

**FITTING PROCEDURE AND EXTRACTED TRENDS** To quantify bromide migration, we use a global fit algorithm. This global fit algorithm is fully described in Sections 3.2.3 and 3.4.3 of Chapter 3. The assumptions of the model are detailed in Chapter 1.

To apply the conversions from  $p_{fit}$  and  $\Delta C(T)$  to  $D(T)$  and  $N_{ion}(T)$ , we need values for the perovskite permittivity  $\epsilon$  and for the doping density  $N_D$  of the devices. These are determined through Mott-Schottky analysis, as shown in Figure 4.6. For typical devices made with small (large) grain size, the perovskite permittivity is of 14.6 (13), while the doping density reaches  $1.13 \times 10^{16} \text{ cm}^{-3}$  ( $4.2 \times 10^{15} \text{ cm}^{-3}$ ).

While fitting the capacitance transients, we find that a biexponential fit works well to describe the data, which supports the hypothesis of two specific ionic contributions, rather than a broad distribution of a single peak<sup>90</sup>. Within each of these migration pathways, however, we cannot completely exclude some distribution in the activation energy and/or diffusion coefficient.

Looking at the results in Figure 4.4, we note that we would expect a reduced diffusion coefficient when the activation energy increases if nothing else changes, contrary to our observation. If we expand the full Equation for the diffusion coefficient  $D_{ion}$ , we find:

$$D_{ion} = \frac{v_a d^2}{6} \exp\left(\frac{\Delta S}{k_B}\right) \exp\left(\frac{-\Delta H}{k_B T}\right)$$

with  $v_a$  the attempt frequency for the ionic jump,  $d$  the ionic jump distance,  $\Delta S$  and  $\Delta H$  the changes in Gibbs free entropy and enthalpy of activation for a single ion migration step<sup>51</sup>.

The combination of an increased activation energy with a constant diffusion coefficient suggests a compensating term when the average grain size is increased: this could be either an increase in the attempt frequency  $v_a$ , an increase in the ionic jump distance  $d$ , or an increase in the entropy term  $\Delta S$ . Regarding the first hypothesis, the presence of uncoordinated atoms in the grain boundary region suggests weaker bonding of the perovskite lattice at these grain boundaries, which is generally related to lower attempt-to-escape frequencies. This would lead indeed to an increase of  $v_a$  with grain size. If we consider the ionic jump distance  $d$ , and follow our previous statement that the defect formation energy is independent of grain size, then  $d$  should remain constant with grain size. On the other hand, at grain boundaries, the higher degrees of freedom suggest that  $\Delta S$  should increase with the amount of grain boundaries, i.e. the trend would consist of a decrease of  $\Delta S$  with grain size. To-

gether, these suggest that the compensating term is an increase of the attempt to escape frequency  $v_a$ .

We note that, as discussed in Section 4.2.1, the extraction layers are chosen specifically because they exhibit no direct ion migration, even though they may reduce the overall PCE of the devices. Ion migration through the extraction layers into the contact layers may still happen on long timescales<sup>157</sup>.

**DLTS MEASUREMENTS** The vacancies necessary for ion migration to occur are part of the wider range of traps and charged point defects that hybrid halide perovskites exhibit<sup>32</sup>. We can study this trap behavior using a deep level transient spectroscopy (DLTS) measurement. DLTS is similar to TID, only the duration of the voltage pulse is shorter, such that traps have enough time to be filled, but ions do not have sufficient time to diffuse<sup>51</sup>. This technique has been extensively used in the past to measure trap state energy and density<sup>158</sup>.

Here we apply a filling pulse of 1 V for a duration of 20 ms to the cells with smallest and largest grain size. The resulting transients are fitted with a global fit procedure, analogous to the one presented for TID.

The fitting function has the same form as Equation 3.1,

$$C(t, T) = C_\infty(T) + \Delta C(T) \exp \left( \frac{-t}{p_{fit} T \exp \left( \frac{E_T}{k_B T} \right)} \right)$$

but now with  $E_T$  the trap depth (replacing the activation energy  $E_a$ ). The only difference lies in the conversion of the factor  $p_{fit}$  to the attempt frequency  $A_0$  relevant for traps, where

$$A_0 = \frac{1}{(p_{fit} \times T^3)}$$

with  $A_0$  the temperature-independent attempt frequency. Often  $A(T) = A_0 T^2$ , the temperature-dependent attempt frequency, is used.

The observation of traps (and not ions) in the DLTS measurements is further confirmed by the fact that the observed trend in DLTS (energy decrease for cells with smallest grain size) is opposite to the one observed in TID for the mobile ions. From this analysis, it also follows that the density of mobile ions is not directly related to the density of traps in the perovskite layer.

Both trap density and trap depth shown in Section 3.2.5 suggest an increased recombination of electrons and holes for the cells with smallest

grain size. On the other hand, the attempt frequency at room temperature  $A(300\text{ K})$  is higher for the devices with smallest grain size, resulting in the following picture: the dense number of deep traps in cells with small grain size can counteract the higher attempt to escape frequency, thereby maintaining a constant level of non-radiative recombination in cells with small and large grain size. This is one possibility to explain the constant  $V_{OC}$  of the devices with respect to grain size. Another possibility is that the constant  $V_{OC}$  is a consequence of an interfacial energetic barrier between the perovskite and one of the transport layers, rather than being determined by the recombination rate - the constant  $V_{OC}$  with regard to grain size would thus be linked to the materials' energetic offset and the resulting interfacial recombination.

#### 4.4.3 MODEL OF ION MIGRATION PATHWAYS

The scheme of migration pathways presented in Figure 4.5 can be further used to estimate key parameters in the bromide migration process at play. Indeed, from the activation energies of peak A in Figure 4.4, we can recover the two underlying activation energies needed for the migration from bulk to grain boundaries, and from grain boundaries to the electrode.

To do so, we use a geometric model as shown in Figure 4.8. Any given bromide ion will travel a distance  $L1$  inside the bulk, then  $L2$  through the grain boundary, here represented as the edge of the rectangle. If the ion starts in position  $(x, y)$ , where  $x$  is the distance between the ion and the electrode in the vertical plane, and  $y$  is the distance between ion and grain boundary in the horizontal plane, then the fraction  $f$  of bulk travelling distance to total travelling distance,  $f = \frac{L1}{L1 + L2}$ , is equal to the following expression:

$$f[v1, v2, L, H] = \frac{\int_0^{x_{max}} dx \int_{y_{min}}^H dy \frac{1}{1 - \frac{v1}{v2} + \frac{y}{x} \sqrt{1 - \left(\frac{v1}{v2}\right)^2}}}{\int_0^{x_{max}} dx \int_{y_{min}}^H dy}$$

with distances as defined in Figure 4.9, where  $x_{max}$  is the minimal value between  $x_{max} = \frac{L}{2}$  and  $x_{max} = \frac{H(v2 - v1)}{\sqrt{v2^2 - v1^2}}$ , and

$y_{min} = x \frac{\sqrt{v2^2 - v1^2}}{v2 - v1}$ . The expression for  $f$  thus takes into account all possible starting values for  $(x, y)$ .

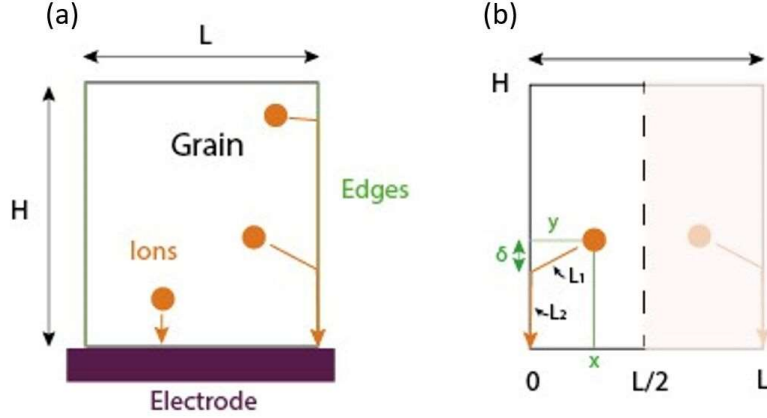


FIGURE 4.9. (a) Geometric scheme showing bromide ions within a perovskite grain for a grain of height  $H$  and length  $L$ , on top of an electrode. The inside of the rectangle represents the bulk of the perovskite lattice, while the edges of the rectangle represent grain boundaries. (b) Mean free path from the grain interior to the electrode of opposite polarity of an ion located at position  $(x, y)$ , with  $L = L_1 + L_2$ ,  $L_1$  being the distance from grain interior to grain boundary, and  $L_2$  from grain boundary to electrode.

The effective activation energy of peak A,  $E_{a(eff)}(A)$  can be written

$$E_{a(eff)}(A) = f E_a(1) + (1 - f) E_a(2)$$

where  $E_a(1)$  and  $E_a(2)$  are the bromide migration activation energies from bulk to grain boundary and from grain boundary to electrode, respectively, where the conversion relation from  $v1$  to  $E_a(1)$ , and from  $v2$  to  $E_a(2)$  are  $v1 = \exp[-E_a(1)]$  and  $v2 = \exp[-E_a(2)]$ . We note that this simplification assumes that the diffusion coefficient for both pathways is identical and only the activation energy is different, as also indicated by our measurement (Figure 4.4d).

We can now estimate  $E_a(1)$  and  $E_a(2)$ , by solving the previous Equation for various sets of  $(E_a(1), E_a(2))$  and try to find the best fit to the activation energies of peak A. The results are shown in Figure 4.10. We note that the x-axis for activation energies of peak A (as shown in Figure 4.4c) is transformed from grain size to a new metric of grain size over thickness of the perovskite layer, allowing to plot all experimental values

on the same axis as the fitted values. The simple model we used predicts a change in the activation energy for aspect ratios between 0 and 2, while our experimental data shows an onset starting around 7.8. The failure to account for the delayed onset of the activation energy change is likely due to the simplicity of our model, which does not account for the distribution of grain sizes in each sample, a possibly rough grain boundary, and for the contribution of a slower diffusion paths to the capacitance decay. Nevertheless, if we shift the x-axis of the model by 7.8, we can reproduce the trend of the activation energy increase as a function of grain aspect-ratio. The plot in Figure 4.5c was obtained with fitted values of the activation energies of 0.50 eV for bulk diffusion and 0.18 eV for grain-boundary diffusion. While not attempting a precise description of the experimental data our model shows the effect that a varying grain size has on the geometry of the ion's path, rationalizing the experimental trend.

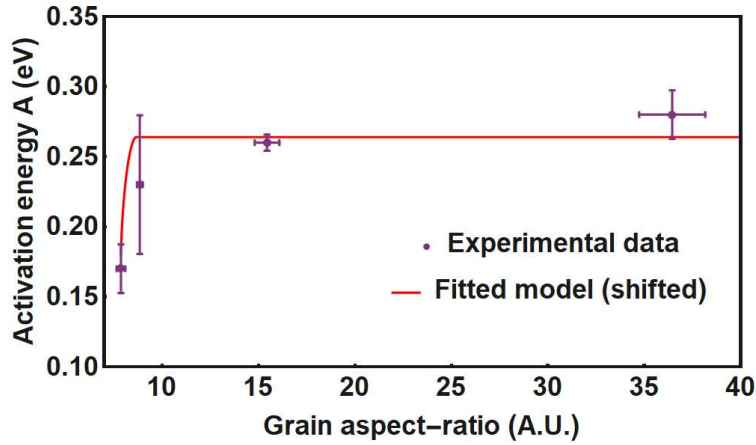


FIGURE 4.10. Experimental activation energies of peak A in purple, rescaled as a function of length over thickness and shifted to lower x-values; fitted geometrical model in red, using values of 0.50 eV for bulk diffusion and 0.18 eV for grain-boundary diffusion. We further note that TID cannot unveil the microscopic pathways of ion diffusion in the perovskite layer, but remains an interesting tool that can be further complemented by theoretical modelling using DFT and MD simulations.